Article ID: 1006-8775(2023)04-0460-13

Zoning Evaluation of Hourly Precipitation in High-resolution Regional Numerical Models over Hainan Island

FENG Xiao (冯 箫)[1,2], WU Yu (吴 俞)[1,2], YANG Wei (杨 薇)[1,2], LI Xun (李 勋)[1,2]
(1. Hainan Provincial Meteorological Observatory, Haikou 570203 China; 2. Key Laboratory of South China Sea Meteorological Disaster Prevention and Mitigation of Hainan Province, Haikou 570203 China)

Abstract: This study assesses the performance of three high-resolution regional numerical models in predicting hourly rainfall over Hainan Island from April to October for the years from 2020 to 2022. The rainfall amount, frequency, intensity, duration, and diurnal cycle are examined through zoning evaluation. The results show that the China Meteorological Administration Guangdong Rapid Update Assimilation Numerical Forecast System (CMA-GD) tends to forecast a higher occurrence of light precipitation. It underestimates the late afternoon precipitation and the occurrence of short-duration events. The China Meteorological Administration Shanghai Numerical Forecast Model System (CMA-SH9) reproduces excessive precipitation at a higher frequency and intensity throughout the island. It overestimates rainfall during the late afternoon and midnight periods. The simulated most frequent peak times of rainfall in CMA-SH9 are 0–1 hour deviations from the observed data. The China Meteorological Administration Mesoscale Weather Numerical Forecasting System (CMA-MESO) displays a similar pattern to rainfall observations but fails to replicate reasonable structure and diurnal variation of frequency-intensity. It underestimates the occurrence of long-duration events and overestimates related rainfall amounts from midnight to early morning. Notably, significant discrepancies are observed in the predictions of the three models for areas with complex terrain, such as the central, southeastern, and southwestern regions of Hainan Island.

Key words: Hainan Island; hourly precipitation; regional numerical model; zoning evaluation
CLC number: P456.7 **Document code:** A
Citation: FENG Xiao, WU Yu, YANG Wei, et al. Zoning Evaluation of Hourly Precipitation in High-resolution Regional Numerical Models over Hainan Island [J]. Journal of Tropical Meteorology, 2023, 29(4): 460-472, https://doi.org/10.3724/j.1006-8775.2023.034

1 INTRODUCTION

The increased atmospheric instability has led to more frequent and severe precipitation events, threatening people's livelihoods and production (Yang et al.[1]; Wu et al.[2]; Brown et al.[3]). Fortunately, significant advancements in detection, assimilation, and numerical modeling technologies have greatly improved the development of high-resolution regional numerical models. These models have proven effective in short-range and nowcasting quantitative precipitation, providing valuable insights into small and mesoscale weather phenomena associated with extreme weather events. However, it is essential to acknowledge that model errors cannot be entirely eradicated. These errors arise from various factors, including initial and boundary conditions, physical processes, and surface accuracy and type (Ding[4]; Boeing[5]). Consequently, achieving precise point, time, and quantity precipitation forecasts based on model outputs remains a big challenge.

In recent years, there has been a growing interest in employing high-resolution regional numerical models for seamless fine-grid weather forecasting (Bi et al.[6]; Jin et al.[7]; Dai et al.[8]; Dai et al.[9]; Wu et al.[10]). Several statistical reprocessing techniques based on these model outputs have been formulated, enhancing precipitation forecast accuracy and aiding the development of intelligent grid weather prediction systems (Hu et al.[11]). A thorough evaluation of the model's strengths and weaknesses is crucial when it comes to utilizing the model for weather prediction and enhancing its performance. This kind of evaluation helps in identifying any systematic biases within the models and in understanding the factors contributing to these inaccuracies (Chakraborty[12]; Mittermaier and Roberts[13]).

Research into the evaluation of model performance, particularly regarding quantitative precipitation forecasting, has become a significant focus. Objective scoring indices such as TS, ETS, and bias have been developed and are commonly utilized to assess the skill of precipitation prediction (Schaefer[14]; Brill and Mesinger[15]; Haiden et al.[16]; Hong[17]). Studies have shown that the ability of models to forecast precipitation varies depending on the model used, atmospheric conditions, and regional geography (Huang and Luo[18]; Mehran and AghaKouchak[19]; Liu et al.[20]). Further

Received 2023-05-04; **Revised** 2023-08-15; **Accepted** 2023-11-15
Funding: Regional Innovation and Development Joint Fund of National Natural Science Foundation of China (U21A6001); China Meteorological Administration Innovation and Development Project (CXFZ2021Z008); Hainan Provincial Meteorological Bureau Business Improvement Project (hnqxSJ202101)
Biography: FENG Xiao, Senior Engineer, primarily researching on tropical precipitation.
Corresponding author: LI Xun, e-mail: cyrilpat@sina.com

performance evaluation that involves zoning tests and weather type categorization could yield more valuable bias information (Zhang et al.[21]). Moreover, assessing the capacity of models to predict hourly precipitation is vital because a model's ability to reproduce physical and thermodynamic weather processes is directly reflected in its ability to predict diurnal variations in precipitation (Yu et al.[22]). Studies focusing on hourly precipitation have shown that overestimation of precipitation frequency can lead to underestimation of precipitation intensity. Also, the precision of simulated precipitation at nighttime tends to be less accurate compared to forecasts made in the afternoon (Brown et al.[23]; Qi et al.[24]; Lu et al.[25]). In mountainous areas or places with steep terrain, deviations in diurnal precipitation patterns are even more pronounced (Li et al.[26]; Yuan et al.[27]).

Hainan Island lies in the tropical region, surrounded by the South China Sea to the south and separated from the north by the Qiongzhou Strait. The island is marked by high terrain in its central and southern areas. From April to October, convective rainfall, influenced by factors such as monsoon troughs, tropical cyclones, land-sea breeze circulation, and the island's unique topography, is prevalent on Hainan Island (Feng et al.[28]; Liang and Wang[29]; Zhu et al.[30]; Zhu et al.[31]). Unfortunately, these rainfall events often lead to meteorological disasters like waterlogging, flooding, and debris flows, posing challenges for the local meteorological service. Several assessments of model performance have been executed to confront these issues (Feng et al.[32]; Wu et al.[33]), including a notable study by Wu et al.[34] that scrutinized hourly-scale precipitation in relation to low-level southerly wind. Despite these studies, certain aspects require further exploration. Our study intends to investigate these untouched areas by adopting a zoning evaluation strategy and concentrating on the frequency, intensity, duration, and diurnal variation of precipitation on an hourly scale. Our objective is to obtain more biased information from three high-resolution regional models concerning warm-season precipitation over Hainan Island. We hope our findings will provide useful insights to enhance local refined precipitation forecasts.

2 DATA AND METHODS

2.1 *Data*

This study draws on quality-controlled hourly precipitation data from 420 rain gauges (Fig. 1) across Hainan Island during the warm seasons (April-October) from 2020 to 2022. The main content is the evaluation of hourly precipitation simulated by three high-resolution regional numerical models, namely CMA-GD, CMA-SH9, and CMA-MESO. These models are commonly employed in local business applications, and their detailed information is presented in Table 1.

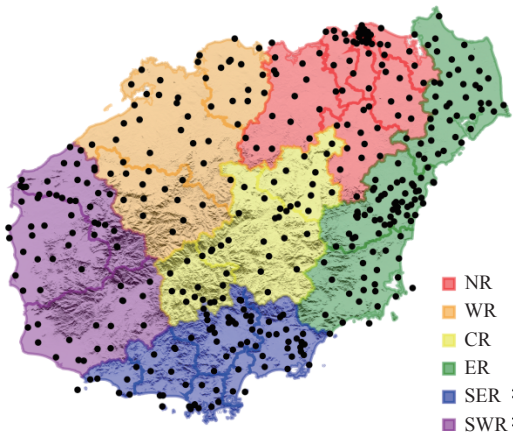


Figure 1. Distribution of 420 observation sites (dotted) across six regions on Hainan Island, with black shading indicating the complex topography. The northern (NR), western (WR), central (CR), eastern (ER), southeastern (SER), and southwestern (SWR) regions are represented by red, orange, yellow, green, blue, and purple patches, respectively.

2.2 *Methods*

To compare with gauge observations, we use bilinear interpolation to interpolate the model grid data to specific stations. To assess the data in more detail, we have divided Hainan Island into six different regions based on both geographical location and administrative divisions. They encompass the northern region (NR), western region (WR), central region (CR), eastern region (ER), southeastern region (SER), and southwestern region (SWR), all of which are depicted in Fig. 1.

In this study, we calculate the mean rainfall amount (mm day^{-1}) by determining the mean rate of cumulative rainfall during all observational hours and multiplying it by 24 h. The hourly precipitation frequency is the ratio of hours with precipitation greater or equal to 0.1 mm per hour. Precipitation intensity is the mean rate of accumulated precipitation during hours with hourly precipitation of 0.1 mm per hour or more. Rainfall events are categorized according to their duration, with a new event being recognized when there is a break in the rain lasting at least two hours (Yu et al.[35]). The duration is defined as the number of hours between the beginning and end of an event. By using each event, we can estimate the diurnal cycles of rainfall events of varying durations. The frequency-intensity structure of precipitation, evaluated by using a double exponential method by Li and Yu[36], can be replaced with a linear equation:

Table 1. Information of high-resolution regional numerical models.

Model System	Model Framework	Resolution	Region
CMA-GD	GRAPES	3 km	16.6°–30.76°N, 96.6°–122.76°E
CMA-SH9	WRF	9 km	7.29969°–59.8497°N, 52.7899°–157.19°E
CMA-MESO	GRAPES	3 km	10°–60.1°N, 70–145°E

$$\ln(\ln(\mathrm{Fr}(I)+1)) = \alpha - \frac{1}{\beta} \quad (1)$$

where I represents the hourly precipitation intensity while $\mathrm{Fr}(I)$ denotes its frequency. The slope and intercept of the fitted line are determined by the parameters α and β, which provide insights into the relationship between frequency and intensity. The diurnal amplitude of rainfall is defined as:

$$\mathrm{AMP} = \frac{R_{\max} - \overline{R}}{\overline{R}} \quad (2)$$

where $R_{\max}$ is the maximum hourly rainfall in a day, and $\overline{R}$ is the daily mean rainfall. In addition, the correlation coefficient (R) and the mean absolute error (MAE) are used to assess the consistency of observed and forecast patterns, as well as the effectiveness of deterministic forecasts for the given region:

$$R = \frac{\sum_{i=0}^{n}(F_i - \overline{F})(O_i - \overline{O})}{\sqrt{\sum_{i=0}^{n}(F_i - \overline{F})^2}\sqrt{\sum_{i=0}^{n}(O_i - \overline{O})^2}} \quad (3)$$

$$\mathrm{MAE} = \frac{1}{n}\sum_{i=0}^{n}|F_i - O_i| \quad (4)$$

where F_i and O_i are the ith values in the forecast and observation field, while n is the number of stations in a specific region.

3 RESULTS

3.1 *Spatial distribution of mean rainfall amount, frequency, and intensity*

Figure 2 displays the mean rainfall pattern obtained from observation and simulation data, along with the discrepancy. The observations reveal a rainfall gradient from east to west, characterized by a larger rainfall center on the eastern windward slope and a smaller one on the western leeward slope (Fig. 2a). While the three regional models mimic this rainfall pattern, they fail to pinpoint the centers or their associated precipitation quantities accurately. For example, CMA-GD misplaces the rainfall center, moving it towards Wanning County in the ER and omitting the western center altogether (Fig. 2b). This discrepancy leads to relatively large negative biases in the CR and positive biases in the SWR (Fig. 2e). Similarly, CMA-SH9 generates excessive precipitation with two rainfall centers that are slightly southward (Fig. 2c). The positive biases spread across the entire island, with the maximum positive biases reaching up to 5.5 mm day^{-1} in the CR and SWR (Fig. 2f). Meanwhile, CMA-MESO can reproduce the pair of rainfall centers, but they are shifted northward. This results in a large area of overestimation in the NR along with underestimation (overestimation) in the CR (SWR) (Fig. 2g). Among the three models, CMA-MESO has the biggest coefficient of pattern correlation with observation and has the most petite MAE over Hainan Island, at 0.896. Conversely, CMA-GD has the lowest correlation coefficient (0.487), and CMA-SH9 has the largest MAE (2.924 mm day^{-1}) (Table 2).

The distribution of hourly precipitation frequency across Hainan Island is presented in Fig. 3. The observed pattern denotes higher frequency values in the eastern part of the island and lower values in the west (Fig. 3a). A high-frequency center is discernable on the east windward slope, aligning with the rainfall distribution in Fig. 2a. However, CMA-GD deviates from the observation, with the frequency center shifting towards the southeast-southwest coastal areas (Fig. 3b). This shift results in a relatively significant overestimation in these areas, with the positive bias being as high as 7.5% in Ledong County in the SWR (Fig. 3e). On the other hand, CMA-SH9's simulated frequency distribution is relatively close to the observation (Fig. 3c), achieving a pattern correlation coefficient of 0.812 (Table 2). Still, it displays positive

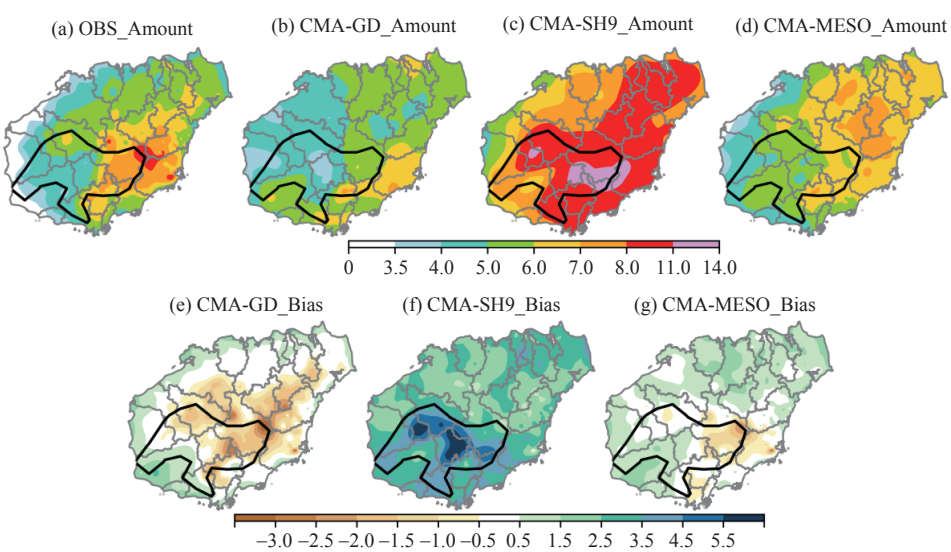


Figure 2. Spatial distribution of mean daily rainfall (shading; units: mm day^{-1}) for observation (a), CMA-GD (b), CMA-SH9 (c), and CMA-MESO (d). The lower panels display the differences (e-g) between model data and observational data (shading; units: mm day^{-1}). The bold black contour delineates a mountainous region with elevations exceeding 400 m.

Table 2. Comparison of spatial correlation coefficients and mean absolute errors between observation and simulation for rainfall amount (units: mm day^{-1}), frequency (%), intensity (units: mm h^{-1}), and duration (units: h) over Hainan Island, including the mean absolute errors of six regions in the island. Bold denotes the biggest MAE among the six regions.

Parameters	Model system	Correlation coefficient	Area mean absolute error						
			NR	WR	CR	ER	SER	SWR	Hainan Island
Amount (mm day^{-1})	CMA-GD	0.487	0.892	0.901	**1.231**	0.842	0.913	0.992	0.935
	CMA-SH9	0.740	2.637	2.605	**3.675**	2.558	3.534	2.896	2.924
	CMA-MESO	0.743	**1.120**	0.884	0.783	0.994	0.564	0.954	0.896
Frequency (%)	CMA-GD	0.437	1.205	1.396	1.306	2.573	**5.507**	3.478	2.649
	CMA-SH9	0.812	2.469	2.268	2.973	3.417	**4.300**	4.065	3.329
	CMA-MESO	0.857	0.847	1.081	1.659	0.964	0.631	**2.073**	1.141
Intensity (mm h^{-1})	CMA-GD	-0.019	0.215	0.295	0.309	0.415	**0.796**	0.497	0.436
	CMA-SH9	0.247	0.421	0.481	**0.606**	0.295	0.295	0.279	0.369
	CMA-MESO	0.020	**0.577**	0.325	0.382	0.460	0.256	0.275	0.391
Duration (h)	CMA-GD	0.044	0.482	0.573	0.622	1.099	**1.653**	0.874	0.946
	CMA-SH9	-0.130	0.186	0.512	0.472	0.197	0.490	**0.916**	0.424
	CMA-MESO	0.487	0.184	0.172	1.231	0.182	0.188	**0.263**	0.199

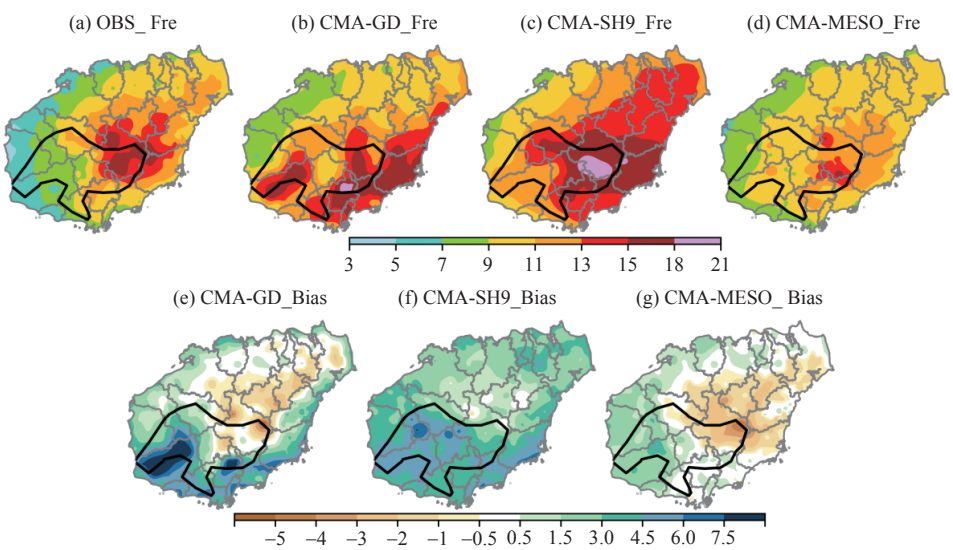


Figure 3. The same as Fig. 2 but for hourly rainfall frequency (shading; %).

deviations that blanket the entire island (Fig. 3f). CMA-MESO also closely mirrors the observed pattern, reaching a pattern correlation coefficient of 0.857. Its frequency biases range between –4.0% and 4.0%, with a relatively minor MAE of 1.141% over Hainan Island. In contrast, CMA-GD and CMA-SH9 exhibit relatively higher MAEs of 2.649% and 3.329%, respectively (Table 2).

Figure 4 illustrates the regional distribution of hourly rainfall intensity over Hainan Island. The intensity pattern seen in Fig. 4a differs from the previously discussed patterns of rainfall amount (Fig. 2a) and frequency (Fig. 3a). Specifically, it portrays lower intensity values in the CR and higher values at the island's periphery. All three models show more significant uncertainty in rainfall intensity, as demonstrated by the relatively low spatial correlation coefficients in Table 2. For example, CMA-GD reveals a relatively weak rainfall intensity in the ER, SER, and SWR with negative biases (Fig. 4e), primarily due to the overestimation of frequency there (Fig. 3e). On the other hand, as presented in Fig. 4f, CMA-SH9 mitigates the overestimation of rainfall intensity in some places, like the ER, SER, and SWR, relative to the rainfall amount (Fig. 2f) or frequency biases (Fig. 3f). However, the intensity biases of CMA-SH9 remain significant in mountainous areas, coinciding with the simulated rainfall amount (Fig. 2f). This result implies that overestimation of rainfall amount over the CR primarily stems from overestimation of rainfall intensity. In contrast, CMA-MESO shows an intensity distribution close to its rainfall amount (Fig. 2d). Regions that display negative intensity biases (Fig. 4g) overlap with areas that reveal positive frequency biases (Fig. 3g), and vice versa. Despite CMA-MESO seemingly surpassing the other two models, CMA-GD and CMA-SH9, in predicting rainfall amounts (Table 2), it is crucial to understand that this outcome is primarily due to the counterbalancing of

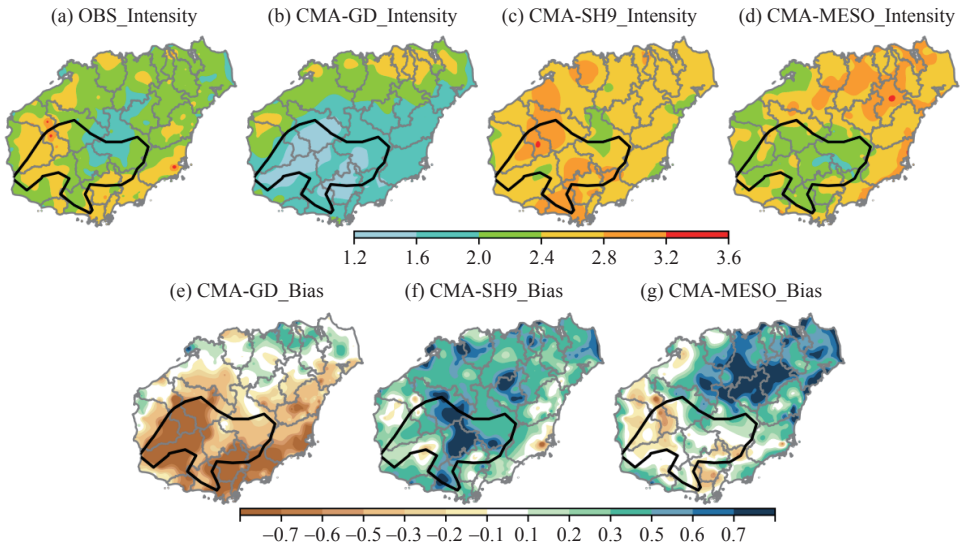


Figure 4. The same as Fig. 2 but for hourly rainfall intensity (shading; units: mm h^{-1}).

frequency and intensity biases inherent in the model.

According to the patterns shown in Fig. 2-4, it is evident that each model delivers different levels of uncertainty in various locations of Hainan Island. Table 2 presents the MAEs that confirm this variation. However, the common thread is that the models usually show greater uncertainty in areas with complex topography, such as the CR, SER, and SWR.

3.2 *Frequency-intensity structure*

Rainfall amounts are composed of varying levels of intensity and frequency. A simulated rainfall pattern that matches the observed pattern does not necessarily prove accurate underlying physical processes. In order to measure the effectiveness of a model in replicating atmospheric processes, it is essential to analyze the relationship between hourly precipitation frequency and rainfall intensity. Figs. 5-7 present the results of this analysis for three models-CMA-GD, CMA-SH9, and CMA-MESO-in six regions. The subgraphs in these figures depict the linear correlation between double logarithmic frequency and rainfall intensity and the deviation between the simulation and observation.

As shown in Fig. 5a, the frequency-intensity curve of CMA-GD in the NR is near that of the observation for

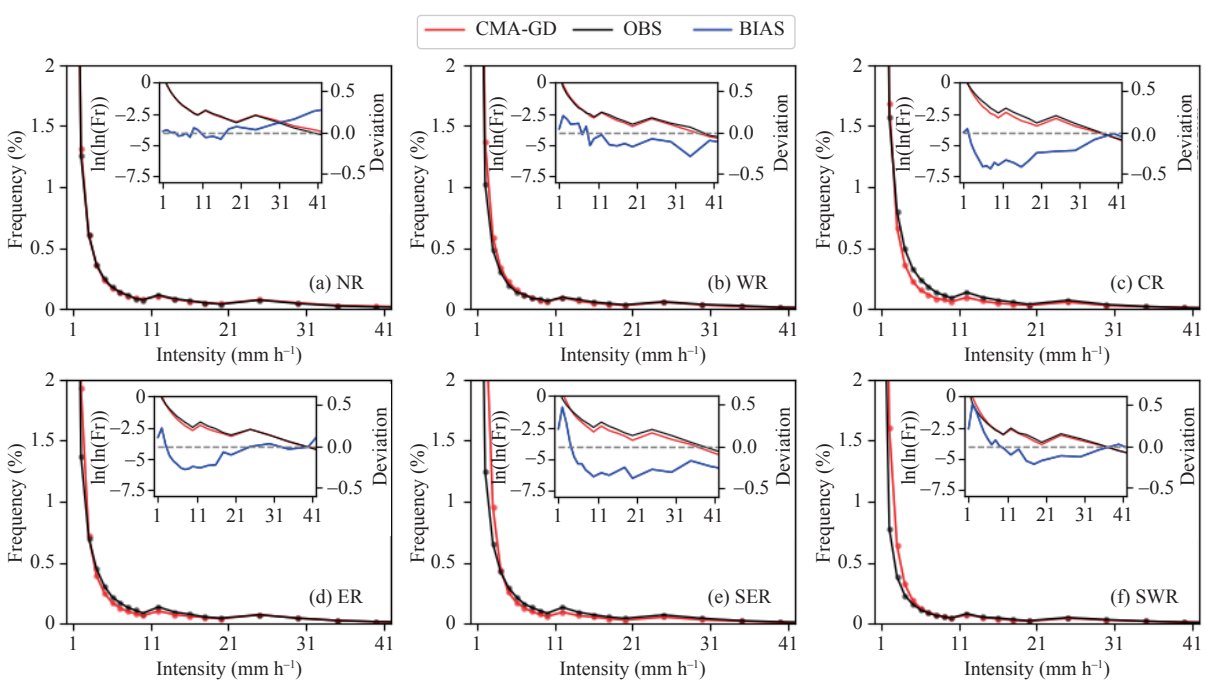


Figure 5. Precipitation frequency (%) and its double logarithm [ln(ln(Fr))] with biases distributed at varying intensities (units: mm h^{-1}) across six regions: (a) NR, (b) WR, (c) CR, (d) ER, (e) SER, and (f) SWR as outlined in Fig. 1. The observation and simulation are represented by black and red lines, respectively, while the blue lines indicate the deviation of [ln(ln(Fr))] between the simulation and observation, dash lines denote zero.

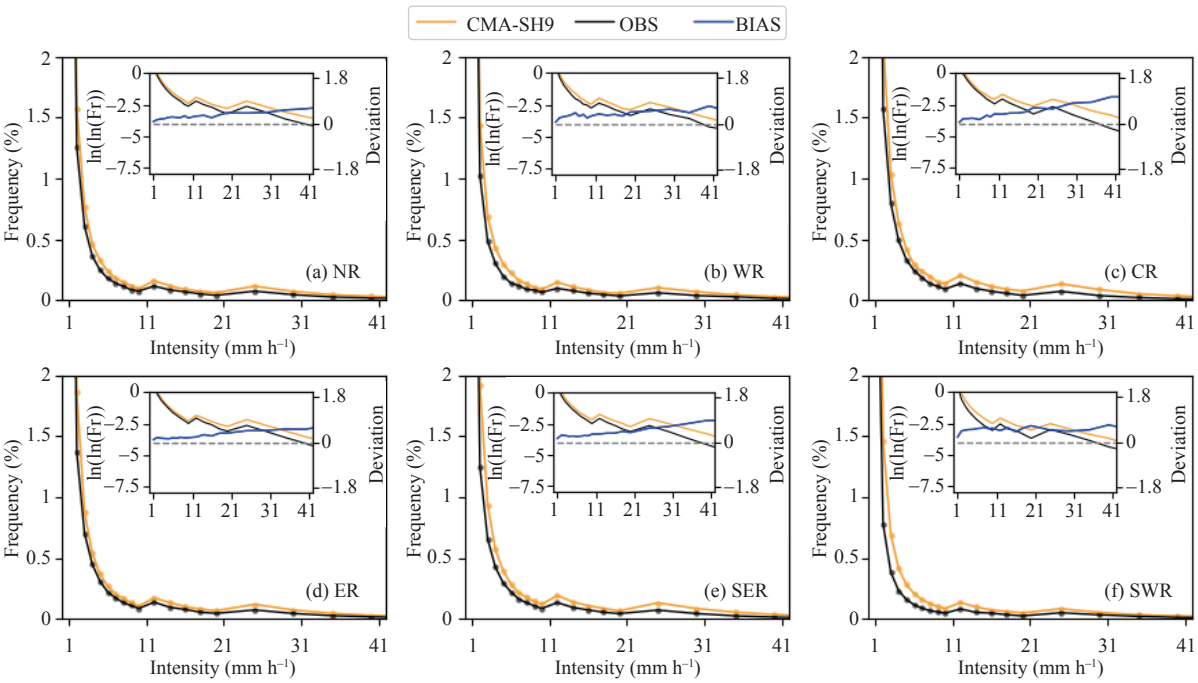


Figure 6. The same as Fig. 5 but for CMA-SH9 with yellow lines.

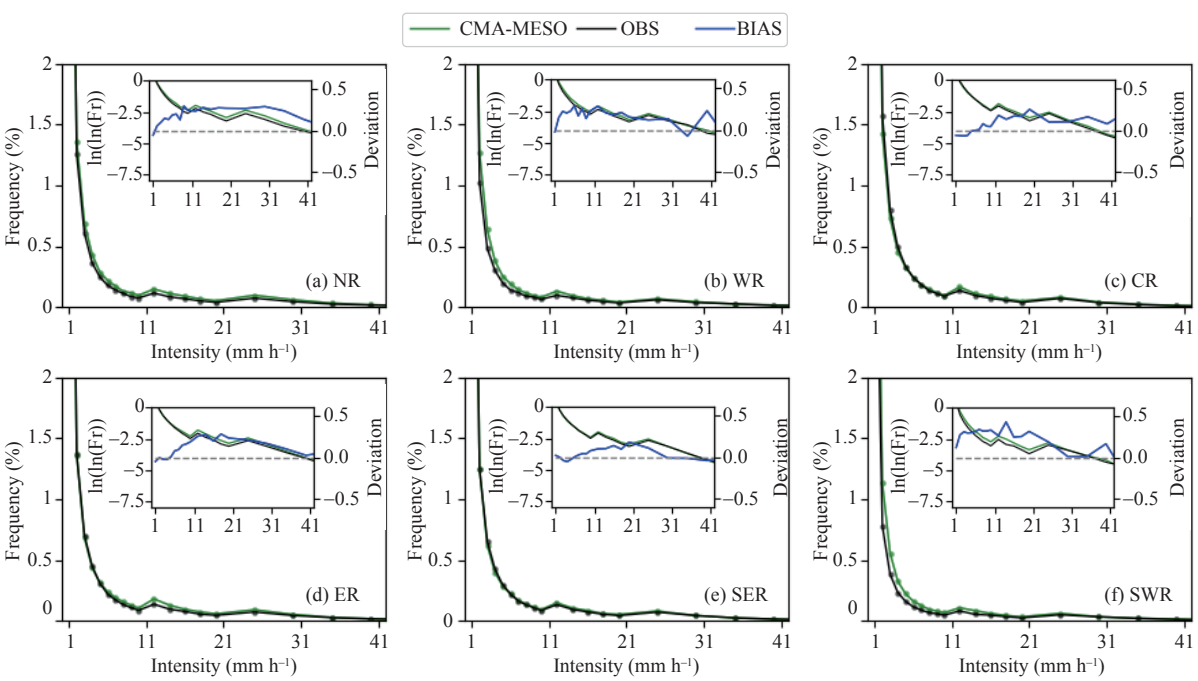


Figure 7. The same as Fig. 5 but for CMA-MESO with green lines.

rainfall intensities below 16 mm h^{-1}. However, the blue deviation line indicates an upward growth trend beyond this point. In other areas, there is a tendency to overestimate hourly frequencies when the intensity is low, transforming into an underestimation as the intensity increases. The transition's critical point varies by region: 8 mm h^{-1} in the WR, 2 mm h^{-1} in the CR, 3 mm h^{-1} in the ER, 4 mm h^{-1} in the SER, and 10 mm h^{-1} in the SWR. Beyond these points, the simulated frequencies (red lines) in the WR and SER continue to be underestimated (Fig. 5b, e). However, at an intensity of 41 mm h^{-1}, the simulated frequencies in the CR, ER, and SWR gradually approach the observed values (black lines) (Fig. 5c, d, f). Notably, in the SER and SWR, the deviation lines (blue lines) for intensities below 5 mm h^{-1} demonstrate a rapid upward and downward motion, implying a relatively significant overestimation of weak precipitation frequencies in these places.

Figure 6 illustrates the frequency-intensity distribution of CMA-SH9. All intensity bins and regions show that the

simulated frequencies (yellow lines) are consistently higher than the observed ones (black lines). This discrepancy explains why CMA-SH9 records a higher rainfall amount MAE than CMA-GD and CMA-MESO (Table 2). Regarding the performance of CMA-MESO (Fig. 7), all regions display analogous features, where the simulated curves coincide with the observed curves at the initial intensity bin and then exceed them as the intensity grows. In certain regions, such as the NR and CR, the deviation lines (blue lines) stay above the zero lines (Fig. 7a, c). In other regions, like the WR, ER, SER, and SWR, the deviation lines gradually approach or fluctuate around the zero lines, particularly at intensity bins of 31–41 mm h^{-1} (Fig. 7b, d, e, f).

Table 3 presents the frequency biases of weak (0.1–4.9 mm h^{-1}), moderate (5.0–19.9 mm h^{-1}), and strong (≥ 20.0 mm h^{-1}) precipitation, aiming to identify the bias features at various intensity levels. Generally speaking, CMA-GD tends to underestimate the frequency of moderate precipitation (negative biases across six regions), whereas CMA-MESO does the opposite. Weak precipitation generates the most noteworthy bias and is the main reason for the overall bias in the regions. Heavy rainfall displays minimal bias, leading to a narrower discrepancy between simulation and observation as the precipitation intensity increases.

3.3 *Precipitation diurnal variation*

Figure 8 displays the hourly precipitation across six regions throughout the day. The ER (SER) demonstrates a bimodal pattern with two peaks occurring at 17:00 (16:00) and 08:00 (04:00) BJT, as indicated by the gray bars in Fig. 8d-e. In contrast, the other regions exhibit an unimodal pattern with a single peak around 17:00 BJT. The NR, WR, CR, and SWR show a more significant diurnal fluctuation than the ER and SER. The diurnal amplitudes measure 1.746, 1.893, 1.162, and 1.876, respectively.

All three models are capable of replicating the day-to-night changes. However, some discrepancies with the observed data persist. CMA-GD tends to underestimate the precipitation amount in the late afternoon, resulting in a lower diurnal amplitude than observed. In the SWR, the simulated amplitude of 0.614 is only a third of the observed amplitude (refer to the red line in Fig. 8f). In

Table 3. The precipitation frequency bias at various intensity levels (%) over the six regions in Hainan Island.

Intensity level	Model system	NR	WR	CR	ER	SER	SWR
Weak (0.1–4.9 mm h^{-1})	CMA-GD	0.250	1.087	–0.271	2.506	5.381	3.477
	CMA-SH9	1.997	1.774	2.186	2.978	3.690	3.490
	CMA-MESO	–0.490	0.258	–1.360	–0.760	0.197	1.818
Moderate (5.0–19.9 mm h^{-1})	CMA-GD	–0.020	–0.031	–0.395	–0.250	–0.282	–0.012
	CMA-SH9	0.325	0.366	0.470	0.304	0.422	0.477
	CMA-MESO	0.258	0.214	0.104	0.226	0.077	0.245
Heavy (≥20.0 mm h^{-1})	CMA-GD	0.027	–0.025	–0.033	0.005	–0.044	–0.008
	CMA-SH9	0.139	0.128	0.202	0.133	0.185	0.097
	CMA-MESO	0.052	0.010	0.016	0.027	–0.001	0.008

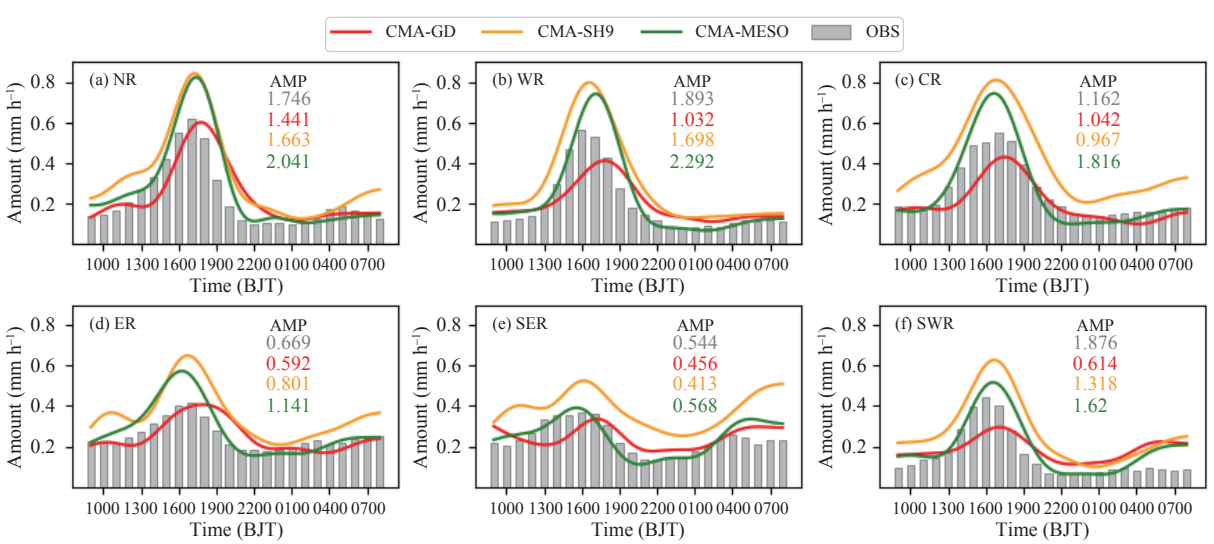


Figure 8. Diurnal variations in rainfall amounts averaged over six regions: (a) NR, (b) WR, (c) CR, (d) ER, (e) SER, and (f) SWR as outlined in Fig. 1. The observation is represented by gray bars while CMA-GD, CMA-SH9, and CMA-MESO are represented by red, yellow and green lines, respectively. The amplitudes of diurnal precipitation for the observation and simulations are depicted with the corresponding colors.

contrast, CMA-SH9 tends to overestimate precipitation during the same period, manifesting a more concentrated, narrower peak. Despite this exaggeration, it does not lead to a larger diurnal amplitude. It can be ascribed to the overestimated rainfall at midnight, which lowers the disparity between $R_{\max}$ and $\overline{R}$ (as seen in Eq. 2), causing a decrease in diurnal amplitude. CMA-MESO overestimates precipitation in the late afternoon, much like CMA-SH9. However, at midnight or in the early morning, CMA-MESO's forecasts roughly match the observed data (excluding the SER and SWR). Therefore, the diurnal amplitude of CMA-MESO is generally larger than the observed values (excluding the SWR).

The variation in precipitation daily is influenced by how frequency and intensity patterns interact. To better understand the diurnal variation of frequency and intensity, quadrant charts are utilized to compare them with observed data (refer to Fig. 9). The *x*-axis and *y*-axis of the graph represent the deviation of frequency and intensity, respectively. The closer the deviations are to the center point, the more reasonable the simulated diurnal variation is. Fig. 9 shows that the bias points deviate from the center relatively far during two specific periods: 13:00–16:00 BJT and 17:00–20:00 BJT. These findings are consistent with the outcomes in Fig. 8, suggesting that considerable biases in rainfall typically transpire during the late afternoon hours. During 13:00-16:00 BJT, the bias points of CMA-GD and CMA-MESO tend to cluster in the first quadrant, indicating frequent occurrences of light rain. In contrast, the bias points for CMA-SH9 during 17:00–20:00 BJT tend to cluster in the second quadrant, implying numerous instances of heavy rainfall. Additionally, there are two periods - from 01:00 to 04:00 BJT and from 05:00 to 08:00 BJT-during which CMA-MESO's bias points appear to fall in the fourth quadrant for most regions, except the SWR. This suggests that, at these times, CMA-MESO frequently overestimates intensity and underestimates frequency.

The most frequent peak times (MFPTs) for observation sites based on precipitation events are analyzed. Boxplots in Fig. 10 illustrate the distribution of MFPTs across six regions. The interquartile ranges for the NR, WR, CR, and SWR are narrow, indicating a limited distribution of observed MFPTs (black box in Fig. 10a-c, f). The mean MFPTs for these regions are 17:00, 16:30, 17:00, and 16:00 BJT, respectively. In contrast, the ER and SER exhibit a broader interquartile range (black box in Fig. 10d-e), indicating a more dispersed range of MFPTs from 07:00 to 16:00 BJT. The mean MFPTs for the ER and SER are 12:00 and 11:00, respectively.

In comparison to the observations, CMA-GD's mean MFPTs tend to be later by 1–2 hours in the NR, WR, and CR (red box in Fig. 10a-c) and earlier by 1–3 hours in the ER, SER, and SWR (red box in Fig. 10d-f). Furthermore, the interquartile range of CMA-GD is narrower in the ER and broader in the SWR, respectively. These findings indicate that CMA-GD may not provide adequate accuracy in forecasting the onset of precipitation peaks in these regions. In the case of CMA-SH9, the simulated mean MFPTs show a high level of consistency with the observed data, with a deviation of only 0–1 hour. The simulated MFPT ranges in most regions align well with the observed data, apart from the SER where the simulated MFPT values are particularly narrow (yellow box in Fig. 10e). The MFPTs of CMA-MESO show a constricted interquartile range in both the ER and SER (green box

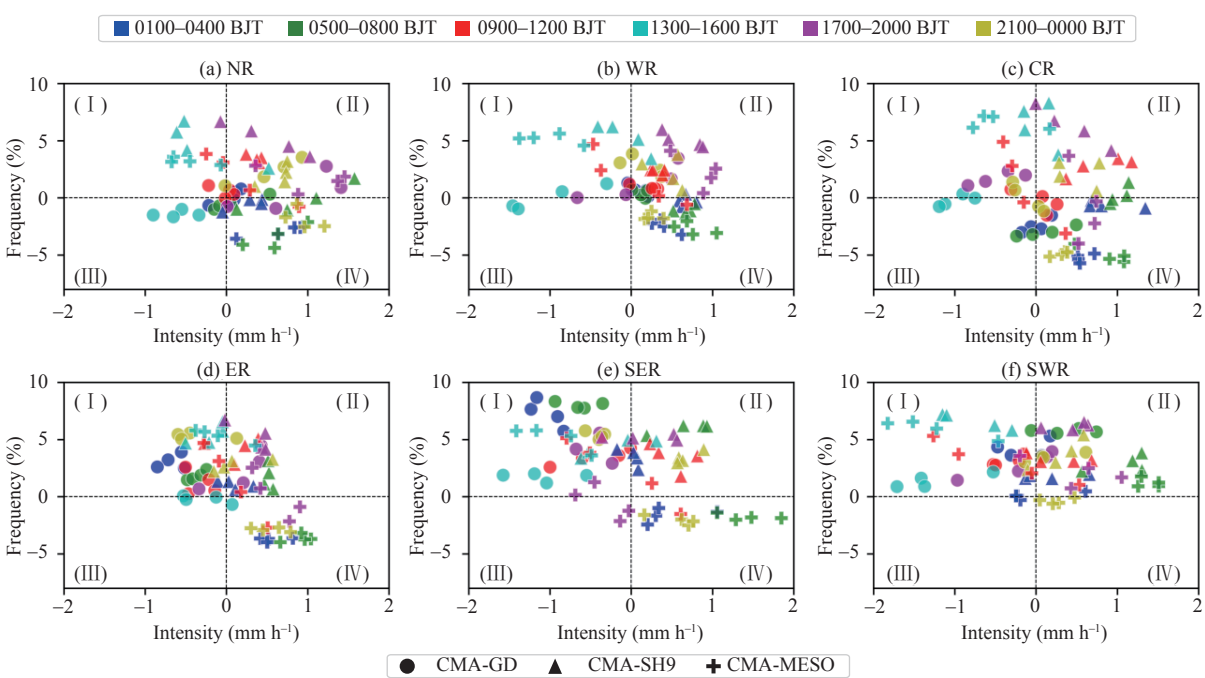


Figure 9. The scatter of (intensity biases and frequency biases) during six periods in a day over the six regions: (a) NR, (b) WR, (c) CR, (d) ER, (e) SER, and (f) SWR as outlined in Fig. 1. with data from CMA-GD (circle), CMA-SH9 (triangle) and CMA-MESO (cross).

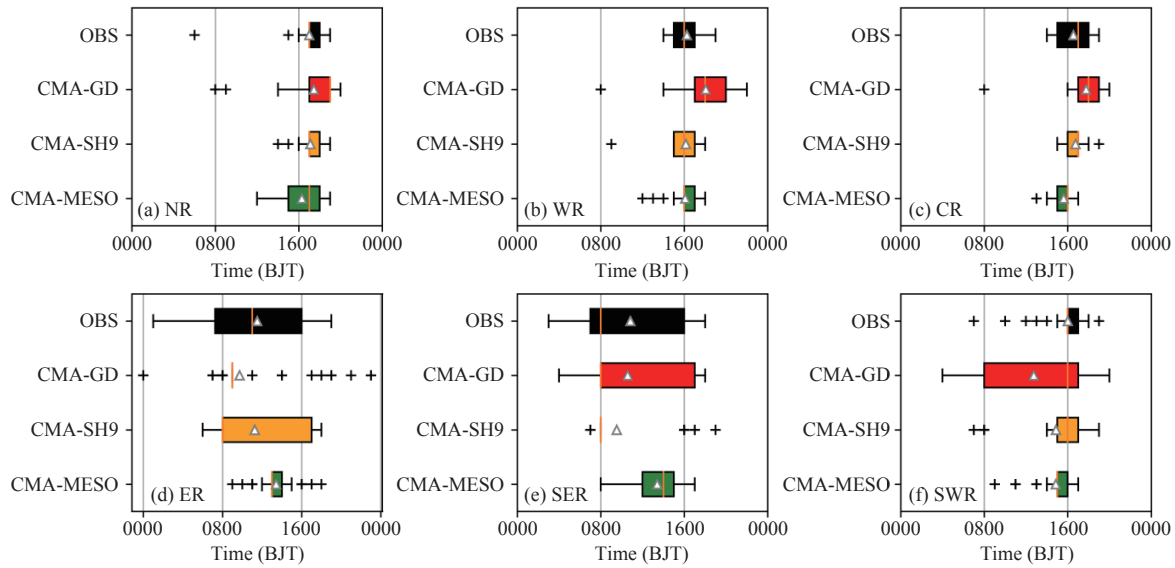


Figure 10. The boxplots of the most frequent peak times of rainfall over the six regions: (a) NR, (b) WR, (c) CR, (d) ER, (e) SER, and (f) SWR as outlined in Fig. 1 with data from the observation (black), CMA-GD (red), CMA-SH9 (yellow) and CMA-MESO (green). The triangles present the mean most frequent peak times of rainfall.

Fig. 10d-e). In these regions, the mean MFPTs are delayed by 2-4 hours compared to the observed values. However, the ranges are dependable elsewhere as the mean MFPTs are only prior by 0–1 hour than the observed values.

3.4 *Precipitation duration*

Figure 11 depicts the spatial distribution of the average precipitation duration calculated by all warm-season precipitation events. The observation reveals that Qiongzhong County, situated in the CR, experiences longer precipitation durations (4.5 to 6.0 hours) than the surrounding areas (3.0 to 4.5 hours). The pattern of precipitation duration in CMA-GD is similar to the simulated frequency (Fig. 3b), unlike that in the observation (Fig. 11a). The pattern correlation coefficient stands at a mere 0.044, primarily due to the more extended duration events occurring in the ER, SER, and SWR. Within these regions, the biggest MAE of 1.653 hours appears in the SER (Table 2). The duration pattern simulated by CMA-SH9 reveals a large value center in the mountainous areas (Fig. 11c), more westward and southward to that of observation. The spatial correlation with the observation is limited at –0.130, which can be attributed to the overestimation (underestimation) of durations in the southern (northern) part of Hainan Island. The CMA-MESO results are generally more consistent with the observation (Fig. 11d), with a spatial correlation coefficient of 0.487 and an MAE of 0.199 hours for the island (Table 2).

To gain a better understanding of the model's ability to simulate precipitation events, we categorized them based on their durations into three groups: short-duration (1–3 hours), medium-duration (4–9 hours), and long-

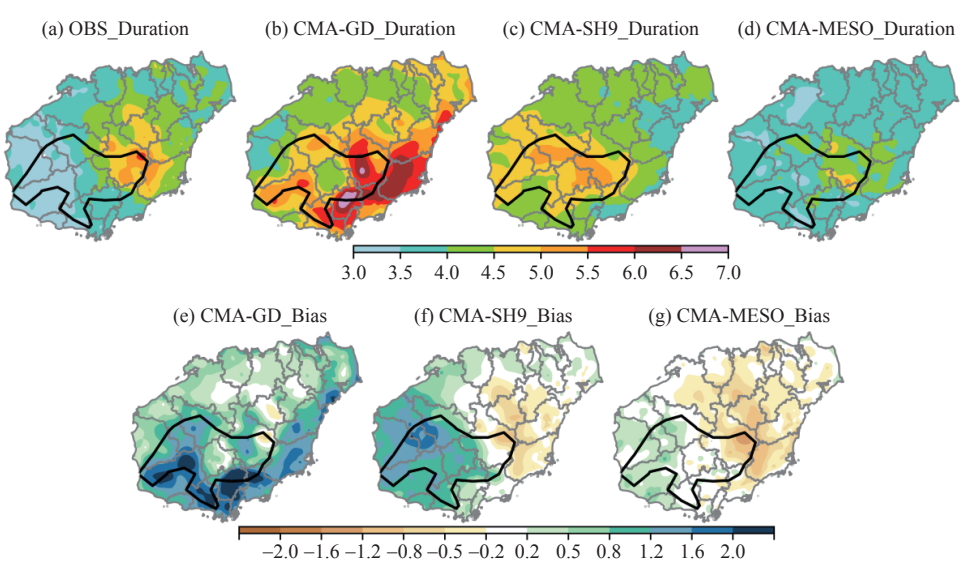


Figure 11. The same as Fig. 2 but for rainfall duration (shading; units: h).

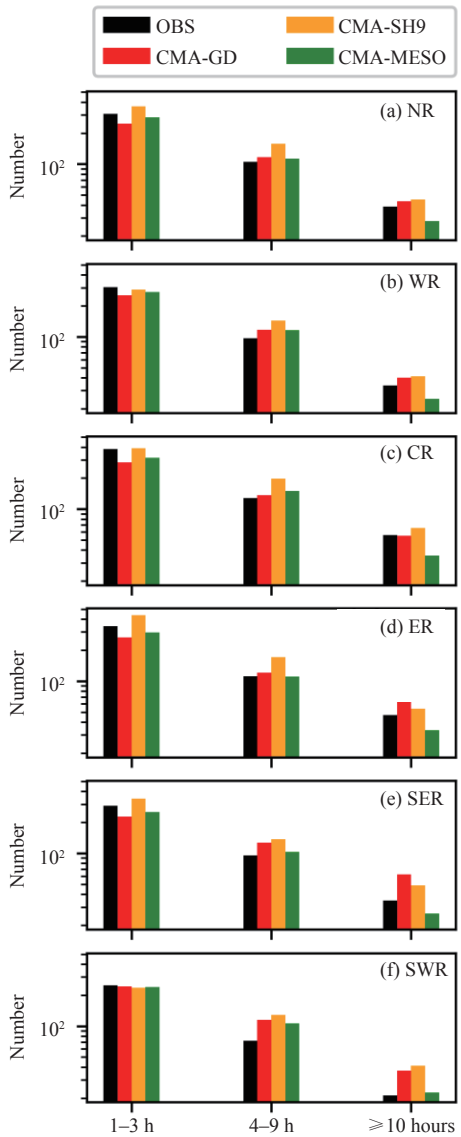


Figure 12. The number of rainfall events with different precipitation durations over six regions: (a) NR, (b) WR, (c) CR, (d) ER, (e) SER, and (f) SWR as outlined in Fig. 1 with data from observation (black), CMA-GD (red), CMA-SH9 (yellow) and CMA-MESO (green).

duration (⩾10 hours). Fig. 12 displays the number of precipitation events and shows that CMA-GD prefers to underestimate short-duration events while overestimating medium- and long-duration events. In particular, the SER and SWR exhibit excessive long-duration precipitation events. These findings correspond to the overestimation of simulated frequency and rainfall duration shown in Fig. 2e and Fig. 11e. CMA-SH9 overestimates the occurrences of short-duration events in the NR, ER, and SER. Also, it overestimates the appearance of medium- and long-duration events in six regions, especially the medium ones. Like CMA-GD, CMA-MESO also underestimates short-duration events and overestimates medium-duration events, but to a lesser extent. Differently, CMA-MESO does not perform well in simulating long-duration events, which are much less frequent than observed in most regions.

Figure 13 shows the observed and simulated diurnal-duration structures of cumulative rainfall amount against the rainfall durations. It can provide implications for the mechanisms of the rainfall process (Yuan et al.[37]). As the observation revealed (Fig. 13a1-a6), there are two types of diurnal cycles against durations: a single afternoon peak of short (1–3 hours)- and medium (4–9 hours)- duration events and double summits of long-duration events (⩾10 hours). The first peak of long-duration events occurs around 12:00–14:00, approximately 3–4 hours earlier than that of short- and medium-duration events (around 17:00). The second peak takes place in the midnight-to-early morning hours and is much more prominent in the ER, SER, and SWR (Fig. 13a4-a6). It is perceivable that the observed MFPTs (Fig. 10) in the NR, WR, ER, and SWR are mainly caused by short- and medium-duration events, whereas in the ER and SER are by long-duration events. Note that while long-duration events are infrequent in the SWR, they can result in considerable precipitation, as shown in Fig. 13a6. When the rainfall duration is between 10 and 15 hours, a significant break in the afternoon's precipitation pattern is apparent in the duration series.

Commonly, the diurnal-duration patterns simulated by CMA-GD, CMA-SH9, and CMA-MESO exhibit similarities with the observed patterns. Nonetheless, for CMA-GD, long-duration events in the ER, SER, and SWR exhibit relatively weak precipitation from midnight to early morning (Fig. 13b4-b6), making it difficult to detect the second peak. Conversely, the SWR exhibits overestimated precipitation during midnight-to-early morning hours for short-duration events (Fig. 13b6), leading to a rise of the red line in Fig. 8f during this time. Afternoon precipitation for short- and medium-duration events is generally underestimated in most regions, with the exception of the NR and CR.

The CMA-SH9 and CMA-MESO models are capable of depicting the double peak phenomenon in long-duration events; however, they are prone to overestimate the quantity of rainfall. This overestimation becomes particularly evident from midnight to early morning in the NR, WR, and CR (as shown in Fig. 13c1-c3 and d1–d3). Furthermore, the short- and medium-duration events also show an overestimation during these hours. Finally, these models fail to accurately portray the discontinuity in rainfall against the duration series in the 10–15 hour range. Concerning peak times, the models show a more skewed movement of the daytime peak, shifting from late afternoon to morning as the duration increases in most regions. This implies that for events of long duration, the peak occurs earlier than the observation. Moreover, CMA-MESO displays an unusual trait in the SER where the values of the nocturnal peak exceed those of the daytime climax (Fig. 13d5). This outcome aligns with the features of green crosses in Fig. 8e and suggests an overestimation of early morning rainfall intensity in CMA-MESO throughout all durations in the SER.

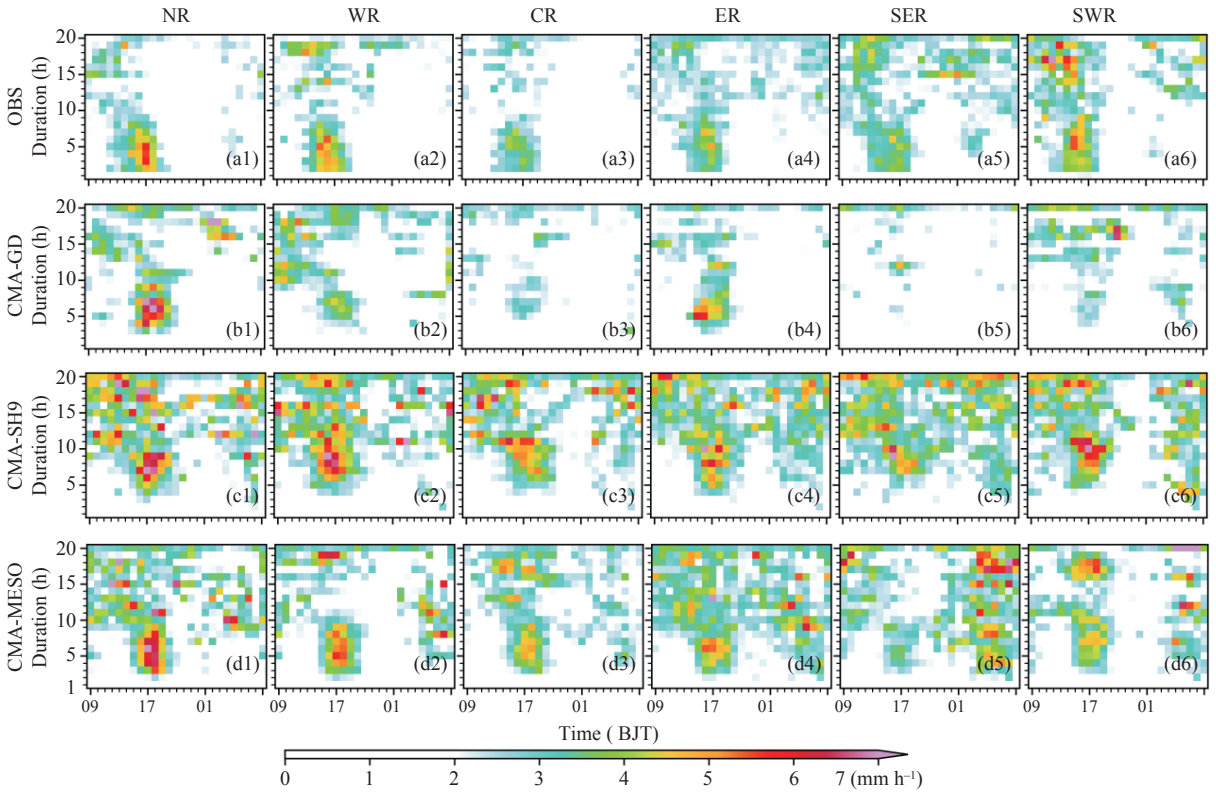


Figure 13. The cumulative summer rainfall amount (shading; units: mm h^{-1}) at different durations (*y*-axis, units: h) and diurnal phases (*x*-axis) averaged over the six regions: NR, WR, CR, ER, SER, and SWR as outlined in Fig. 1 with data from observation (a1-a6), CMA-GD (b1-b6), CMA-SH9 (c1-c6) and CMA-MESO (d1-d6).

4 CONCLUSION

The object of our study is to evaluate how well three high-resolution regional numerical models can reproduce warm-season precipitation over Hainan Island at an hourly scale. CMA-GD, CMA-SH9, and CMA-MESO are these models. To accomplish this, we divide Hainan Island into six separate regions before applying zoning evaluation and quantitatively analyzing the frequency, intensity, duration, and diurnal variation of the hourly precipitation in all regions. Based on the study, we draw the following main conclusions:

(1) Compared to the observations, CMA-GD depicts a large-value center to the east and south in the distribution of rainfall amounts and frequencies and tends to simulate more light rainfall, particularly in the SER and SWR. Short- (medium- and long-) duration precipitation events are underestimated (overestimated) by CMA-GD. In most regions, the afternoon precipitation brought by short-duration events is underestimated, as well as the rainfall from midnight to early morning caused by long-duration events in the ER, SER, and SWR.

(2) CMA-SH9 generates more precipitation with higher frequency and intensity throughout Hainan Island than the observation. The CR experiences the highest MAE in terms of both rainfall amount and intensity. CMA-SH9 reproduces the mean MFPTs, basically matching the observed data. However, it tends to overestimate the occurrence of medium- and long-duration events, with considerably overestimated precipitation in the late afternoon and midnight.

(3) Although CMA-MESO can display a similar pattern to the observations regarding rainfall amount, frequency, and duration, it cannot reproduce a reasonable structure and diurnal variation of frequency-intensity, in addition to the diurnal cycles of rainfall versus the duration phase. CMA-MESO tends to underestimate the occurrence of long-duration events while overestimating the related rainfall amount from midnight to early morning. This is particularly evident in the SER, where nighttime peak values surpass daytime peak values across all durations.

In conclusion, the findings indicate that CMA-GD, CMA-SH9, and CMA-MESO exhibit more significant uncertainty when assessing hourly precipitation. Various models demonstrate varying biases across regions of Hainan Island, especially in regions with complex terrain like CR, SER, and SWR. Therefore, it is crucial to take note of the discrepancies presented in this paper when applying high-resolution regional numerical models for practical purposes. Future research will investigate underlying factors contributing to model biases to enhance weather forecasting and climate research on Hainan Island.

REFERENCES

[1] YANG H, ZHOU W, WANG X K, et al. Analysis on Extremity and characteristics of the “21·7” severe torrential rain in Henan Province [J]. Meteorological Monthly,

2022, 48(5): 571-579, https://doi.org/10.7519/j.issn.1000-0526.2021.111201, in Chinese with English abstract

[2] WU M W, LUO Y L, CHEN F, et al. Observed link of extreme hourly precipitation changes to urbanization over coastal South China [J]. Journal of Applied Meteorology and Climatology, 2019, 58(8): 1799-1819, https://doi.org/10.1175/JAMC-D-18-0284.1

[3] BROWN V M, KEIM B D, BLACK A W. Climatology and trends in hourly precipitation for the Southeast United States [J]. Journal of Hydrometeorology, 2019, 20(8): 1737-1755, https://doi.org/10.1175/JHM-D-19-0004.1

[4] DING Y H. Advanced Synoptic Meteorology [M]. Beijing: China Meteorological Press, 2005: 770-789 (in Chinese)

[5] BOEING G. Visual analysis of nonlinear dynamical systems: chaos, fractals, self-similarity and the limits of prediction [J]. Systems, 2016, 4(4): 37, https://doi.org/10.31219/osf.io/c7p43

[6] BI B G, DAI K, WANG Y, et al. Advances in techniques of quantitative precipitation forecast [J]. Journal of Applied Meteorological Science, 2016, 27(5): 534-549, https://doi.org/10.11898/1001-7313.20160503, in Chinese with English abstract

[7] JIN R H, DAI K, ZHAO R X, et al. Progress and challenge of seamless fine gridded weather forecasting technology in China [J]. Meteorological Monthly, 2019, 45(4): 445-457, https://doi.org/10.7519/j.issn.1000-0526.2019.04.001, in Chinese with English abstract

[8] DAI K, CAO Y, QIAN Q F, et al. Situation and tendency of operational technologies in short and medium range weather forecast [J]. Meteorological Monthly, 2016, 42(12): 1445-1455, https://doi.org/10.7519/j.issn.1000-0526.2016.12.002, in Chinese with English abstract

[9] DAI K, ZHU Y J, BI B G. The review of statistical post-process technologies for quantitative precipitation forecast of ensemble prediction system [J]. Acta Meteorologica Sinica, 2018, 76(4): 493-510, https://doi.org/10.11676/qxxb2018.015, in Chinese with English abstract

[10] WU Q S, HAN M, LIU M, et al. A comparison of optimal-score-based correction algorithms of model precipitation prediction [J]. Journal of Applied Meteorological Science, 2017, 28(3): 306-317, https://doi.org/10.11898/1001-7313.20170305, in Chinese with English abstract

[11] HU Z G, XUE F, JIN R H, et al. Design and implementation of gridded forecast application analysis platform [J]. Meteorological Monthly, 2020, 46(10): 1340-1350, https://doi.org/10.7519/j.issn.1000-0526.2020.10.008, in Chinese with English abstract

[12] CHAKRABORTY A. The skill of ECMWF medium-range forecasts during the year of tropical convection 2008 [J]. Monthly Weather Review, 2010, 138(10): 3787–3805, https://doi.org/10.1175/2010MWR3217.1

[13] MITTERMAIER M, ROBERTS N. Intercomparison of spatial forecast verification methods: Identifying skillful spatial scales using the fractions skill score [J]. Weather and Forecasting, 2010, 25(1): 343-354, https://doi.org/10.1175/2009WAF2222260.1

[14] SCHAEFER J T. The critical success index as an indicator of warning skill [J]. Weather and Forecasting, 2010, 5(4): 570–575, https://doi.org/10.1175/1520-0434(1990)005<0570:TCSIAA>2.0.CO;2

[15] BRILL K F, MESINGER F. Applying a general analytic method for assessing bias sensitivity to bias-adjusted threat and equitable threat scores [J]. Weather and Forecasting, 2009, 24(6): 1748–1754, https://doi.org/10.1175/2009WAF2222272.1

[16] HAIDEN T M, RODWELL M J, RICHARDSON D S. Intercomparison of global model precipitation forecast skill in 2010/11 using the SEEPS score [J]. Monthly Weather Review, 2012, 140(8): 2720–2733, https://doi.org/10.1175/MWR-D-11-00301.1

[17] HONG J S. Evaluation of the high-resolution model forecasts over the Taiwan area during GIMEX [J]. Weather and Forecasting, 2003, 18(5): 836–846, https://doi.org/10.1175/1520-0434(2003)018,0836:EOTHMF.2.0.CO;2

[18] HUANG L, LUO Y. Evaluation of quantitative precipitation forecasts by TIGGE ensembles for south China during the presummer rainy season [J]. Journal of Geophysical Research: Atmospheres, 2017, 122(16): 8494–8516, https://doi.org/10.1002/2017JD026512

[19] MEHRAN A, AGHAKOUCHAK A, PHILLIPS T J. Evaluation of CMIP5 continental precipitation simulations relative to satellite-based gauge-adjusted observations [J]. Journal of Geophysical Research: Atmospheres, 2014, 119 (4): 1695–1707, https://doi.org/10.1002/2013JD021152

[20] LIU C, SUN J H, YANG X L, et al. Evaluation of ECMWF precipitation predictions in China during 2015-18 [J]. Weather and Forecasting, 2021, 36(3): 1043-1060, https://doi.org/10.1175/WAF-D-20-0143.1

[21] ZHANG G H, ZHANG J T, ZHANG N, et al. The NWP models' evaluation Based on different weather type in Hebei [J]. Meteorological Monthly, 2011, 37(8): 968-976, https://doi.org/10.7519/j.issn.1000-0526.2011.8.008

[22] YU R C, LI W, ZHANG X H, et al. Climatic features related to eastern China summer rainfalls in the NCAR CCM3 [J]. Advances in Atmospheric Sciences, 2000, 17: 503–518, https://doi.org/10.1007/s00376-000-0014-9

[23] BROWN J R, JAKOB C, HAYNES J M. An evaluation of rainfall frequency and intensity over the Australian region in a global climate model [J]. Journal of Climate, 2010, 23 (24): 6504–6525, https://doi.org/10.1175/2010JCLI3571.1

[24] ZHONG Q, SUN Z, CHEN H M, et al. Multi model forecast biases of the diurnal variations of intense rainfall in the Beijing-Tianjin-Hebei region [J]. Science China Earth Science, 2022, 65: 1490–1509, https://doi.org/10.1007/s11430-021-9905-4

[25] LU B, SUN J S, ZHONG J Q, et al. Analysis of characteristic bias in diurnal precipitation variation forecasts and possible reasons in a regional forecast system over Beijing area [J]. Acta Meteorologica Sinica, 2017, 75 (2): 248-259, https://doi.org/10.11676/qxxb2017.021, in Chinese with English abstract

[26] LI N N, LI J, RONG X Y, et al. Obtaining more information about precipitation biases over East Asia from hourly-scale evaluation of model simulation [J]. Journal of Meteorological Research, 2020, 34(3): 515–528, https://doi.org/10.1007/s13351-020-9147-1

[27] YUAN W H, HU X L, LI Y S. Evaluation of the hourly rainfall in the ECMWF forecasting over southwestern China [J]. Meteorological Applications, 2020, 27(4): e1936, https://doi.org/10.1002/met.1936

[28] FENG X, WU R G, CHEN J P, et al. Factors for interannual variations of September–October rainfall in Hainan,

China [J]. Journal of Climate, 2013, 26(22): 8962-8978, https://doi.org/10.1175/JCLI-D-12-00728.1

[29] LIANG Z, WANG D. Sea breeze and precipitation over Hainan Island [J]. Quarterly Journal of the Royal Meteorological Society, 2017, 143(702): 137-151, https://doi.org/10.1002/qj.2952

[30] ZHU L, CHEN X C, BAI L Q. Relative roles of low-level wind speed and moisture in the diurnal cycle of rainfall over a tropical island under monsoonal flows [J]. Geophysical Research Letters, 2020, 47(8): e2020GL087467, https://doi.org/10.1029/2020GL087467

[31] ZHU L, MENG Z Y, ZHANG F Q, et al. The influence of sea- and land-breeze circulations on the diurnal variability in precipitation over a tropical island [J]. Atmospheric Chemistry and Physics, 2017, 17(21): 13213-13232, https://doi.org/10.5194/acp-17-13213-2017

[32] FENG X, WU Y, LI Y M, et al. Verification of grid sunny/rainy forecast in Hainan Island based on gridded observation data [J]. Journal of Tropical Meteorology, 2022, 38(1): 91-100, https://doi.org/10.16032/j.issn.1004-4965.2022.009, in Chinese with English abstract

[33] WU Y, FENG X, LI X, et al. Evaluation of spatio-temporal parameters of forecasts from GRAPES_GZ3km model with specific reference to non-typhoon precipitation during the warm season in 2019 in Hainan Island [J]. Journal of Tropical Meteorology, 2021, 37(4): 633-646, https://doi.org/10.16032/j.issn.1004-4965.2021.060, in Chinese with English abstract

[34] WU Y, LI Y M, LI X, et al. Verification of precipitation refinement forecast of regional numerical models in the warm season of Hainan Island [J]. Meteorological Monthly, 2023, 49(2): 235-248, https://doi.org/10.7519/j.issn.1000-0526.2022.110801, in Chinese with English abstract

[35] YU R C, ZHOU T J, XIONG A Y, et al. Diurnal variations of summer precipitation over contiguous China [J]. Geophysical Research Letters, 2007, 34: L01704, https://doi.org/10.1029/2006GL028129

[36] LI J, YU R. A method to linearly evaluate rainfall frequency-intensity distribution[J]. Journal of Applied Meteorology and Climatology, 2014, 53(4): 928–934, https://doi.org/10.1175/JAMC-D-13-0272.1

[37] YUAN W H, YU R C, CHEN H M, et al. Subseasonal characteristics of diurnal variation in summer monsoon rainfall over central eastern China [J]. Journal of Climate, 2010, 23: 6684–6695, https://doi.org/10.1175/2010JCLI3805.1

Citation: FENG Xiao, WU Yu, YANG Wei, et al. Zoning Evaluation of Hourly Precipitation in High-resolution Regional Numerical Models over Hainan Island [J]. Journal of Tropical Meteorology, 2023, 29(4): 460-472, https://doi.org/10.3724/j.1006-8775.2023.034